

# Demographic-aware fine-grained visual recognition of pediatric wrist pathologies

Ammar Ahmed<sup>1</sup>[0009-0003-9984-4819], Ali Shariq Imran<sup>1</sup>[0000-0002-2416-2878],  
Zenun Kastrati<sup>2</sup>[0000-0002-0199-2377], and Sher Muhammad  
Daudpota<sup>3</sup>[0000-0001-6684-751X]

<sup>1</sup> Department of Computer Science (IDI), Norwegian University of Science & Technology (NTNU), Gjøvik, 2815, Norway  
ammaa@stud.ntnu.no, ali.imran@ntnu.no

<sup>2</sup> Department of Informatics, Linnaeus University, Växjö, 351 95, Sweden  
zenun.kastrati@lnu.se

<sup>3</sup> Department of Computer Science, Sukkur IBA University, Sukkur, 65200, Pakistan  
sher@iba-suk.edu.pk

**Abstract.** Pediatric wrist pathologies recognition from radiographs is challenging because normal anatomy changes rapidly with development: evolving carpal ossification and open physes can resemble pathology, and maturation timing differs by sex. Image-only models trained on limited medical datasets therefore risk confusing normal developmental variation with true pathologies. We address this by framing pediatric wrist diagnosis as a fine-grained visual recognition (FGVR) problem and proposing a demographic-aware hybrid convolution–transformer model that fuses X-rays with patient age and sex. To leverage demographic context while avoiding shortcut reliance, we introduce progressive metadata masking during training. We evaluate on a curated dataset that mirrors the typical constraints in real-world medical studies. The hybrid FGVR backbone outperforms traditional and modern CNNs, and demographic fusion yields additional gains. Finally, we show that initializing from a fine-grained pretraining source improves transfer relative to standard ImageNet initialization, suggesting that label granularity, even from non-medical data, can be a key driver of generalization for subtle radiographic findings.

**Keywords:** Pediatric fractures · fracture detection · wrist pathologies · fine-grained classification · Multimodal fusion

## 1 Introduction

Wrist fractures represent up to 75% of hand injuries in emergency departments and pose a significant risk of long-term impairment if misdiagnosed [1]. Given the wrist’s complex anatomy and developmental variability, accurate radiographic interpretation is essential. Recent advances in computer vision have demonstrated promise for automated abnormality detection in musculoskeletal imaging [2]. However, such methods typically rely on large, labeled datasets, which are

scarce in medical domains, and often process X-rays without contextual patient information.

To overcome the limitations of image-only learning, related work in multi-modal frameworks that fuse patient metadata with imaging have been successfully applied in dermatology and oncology domains. Studies have shown consistent accuracy improvements by incorporating age, sex, and anatomical site information images [3–6]. For example, Thomas et al. [6] fused demographic variables with dermoscopy images, while Cai et al. [5] applied ViTs with metadata encoders, achieving 93.8% melanoma classification accuracy. Recently, Hinterwimmer et al. [7] extended this approach to musculoskeletal imaging, reporting gains in bone tumour classification by integrating X-rays and metadata. Despite these advances, metadata integration has not been systematically investigated for wrist pathology recognition.

Pediatric wrist radiographs are particularly challenging because anatomy changes rapidly with development: open physes and progressive carpal ossification can mimic pathology, and maturation differs by sex [8–10]. This yields small inter-class differences (subtle fractures vs. normal irregularities) and large intra-class variation, closely matching the conditions of fine-grained visual recognition (FGVR) [11, 12]. We therefore study pediatric wrist recognition under three hypotheses: **H1**: FGVR-style hybrid convolution–transformer architectures outperform purely convolutional baselines, including modern CNNs such as ConvNeXt [13] (and detection-based baselines such as YOLO [14]), under matched training settings. **H2**: Fusing age and sex improves accuracy and robustness by providing developmental context. **H3**: Fine-grained pretraining transfers better than ImageNet pretraining because it encourages representations sensitive to subtle visual differences [15]. Our contributions are as follows:

1. **FGVR inductive bias for pediatric wrists**: We argue and empirically test that pediatric wrist abnormality recognition is well-modeled as an FGVR problem under strong developmental variation.
2. **Demographic-aware multimodal model**: We use a fusion strategy that integrates age and sex while discouraging shortcut learning via progressive metadata masking.
3. **Fine-grained pretraining**: We show that fine-grained non-medical pretraining improves transfer relative to ImageNet initialization.

## 2 Methods

### 2.1 Dataset Curation & Patient Metadata

We curated two classification datasets derived from GRAZPEDWRI-DX dataset [16]. The dataset comprises 20,327 wrist radiographs from 6,091 pediatric patients with a mean age of 10.9 years (range 0.2–19 years) with 2,688 females, 3,402 males, and one patient with unknown sex. The images include both posteroanterior and lateral projections. GRAZPEDWRI-DX spans nearly the full pediatric age range from infancy to late adolescence. This wide coverage captures

multiple stages of skeletal development, including progressive carpal ossification and age-dependent changes in the distal radius/ulna physis.

Table 1: Instances in training, validation, and test sets from the curated datasets.

<b>Three Wrist Pathologies (Limited set)</b>			
Class	Training	Validation	Test
Boneanomaly	392	98	119
Fracture	400	100	120
Soft-tissue	376	94	115
Total	1168	292	354
<b>Fracture vs. No Fracture (Entire set)</b>			
Class	Training	Validation	Test
Fracture	11854	1357	338
No Fracture	10164	1357	338
Total	22018	2714	676

The first curated dataset is a limited three-class pathology subset comprising fracture, bone anomaly, and soft-tissue abnormality. All other labels were excluded because, after restricting the instances with exactly one pathology label per image (to avoid multi-label ambiguity), the remaining classes contained too few examples for reliable training. The second curated dataset is a binary “Fracture vs. No Fracture” that uses the full set of available images. Final dataset splits are reported in Table 1. Figure 1 summarizes demographic distributions across pathologies.

## 2.2 Preprocessing and Augmentation

All radiographs are resized to  $224 \times 224$ . To improve robustness to acquisition variability, we apply training-time augmentation with Keras `ImageDataGenerator`: rotations ( $\pm 15^\circ$ ), width/height shifts (0.2/0.1), shear (0.2), zoom (0.1), and brightness jitter (0.7, 1.3). We additionally use ZCA whitening and constant padding for empty regions (`fill_mode="constant"`).

```

rotation_range = 15,
width_shift_range = 0.2,
height_shift_range = 0.1,
horizontal_flip = True,
shear_range = 0.2,
brightness_range = (0.7, 1.3),
zoom_range = 0.1,
fill_mode = "constant",
zca_whitening = True.

```

We chose these values to provide effective regularization without introducing unrealistic transformations that could move relevant anatomy out of frame or substantially distort exposure.

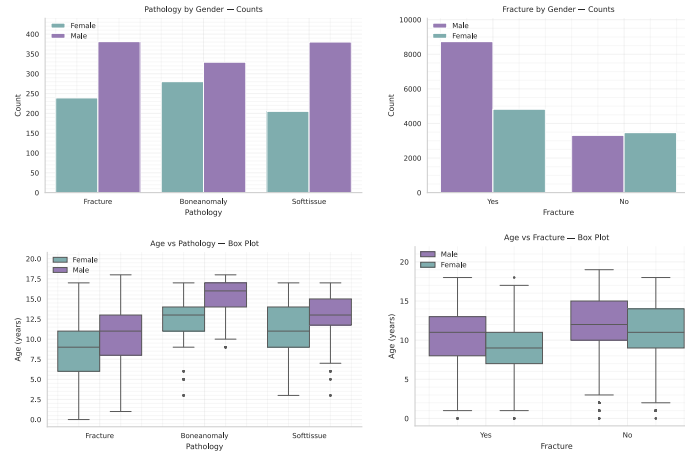


Fig. 1: Bar and box plots for gender and age, respectively, for both curated datasets.

### 2.3 Architectural Details

This work utilizes a hybrid architecture that integrates both visual data and meta-information, drawing inspiration from the base MetaFormer architecture [17]. As depicted in Fig. 2, the architecture is organized into five stages. The first stage (S0) starts with a basic 3-layer convolutional stem, which processes raw input images. Subsequent stages progressively downsample the feature maps and increase channel dimensionality. Stages S1 and S2 consist of MBCConv blocks enhanced with squeeze-and-excitation mechanism. The final two stages, S3 and S4, transition to transformer-based blocks that employ relative positional encoding. This design allows the model to capture global dependencies, which are crucial for subtle pathological differences that span larger contexts (e.g., comparing radius vs. ulna contours or detecting diffuse soft tissue swelling).

Downsampling is applied at the beginning of each stage. In S3 and S4, overlapping patch embedding is implemented using convolutions with a stride of 2 and zero-padding, effectively reducing resolution while maintaining contextual overlap. Table 2 outlines the configuration details of the three variants of the architecture used in our experiments.

To overcome the lack of spatial awareness in standard self-attention, the model incorporates a relative position bias. Specifically, a bias matrix  $B \in$

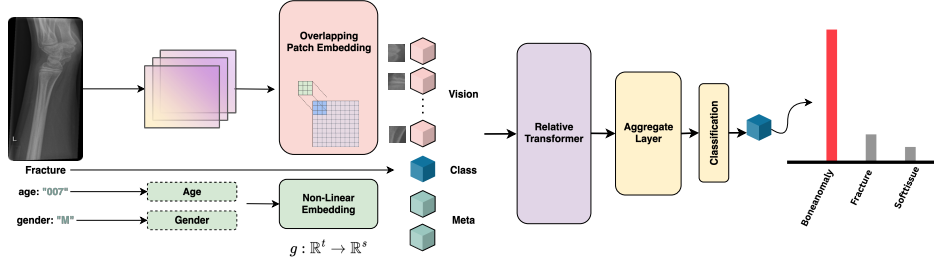


Fig. 2: The architecture pipeline integrates visual, class, and meta tokens within a transformer framework.

Table 2: Configuration of the architecture stages employed in this study. B: number of blocks, and H: hidden dimensions for each stage.

Stage	FG-0	FG-1	FG-2
S0	B=3 H=64	B=3 H=64	B=3 H=128
S1	B=2 H=96	B=2 H=96	B=2 H=128
S2	B=3 H=192	B=6 H=192	B=6 H=256
S3	B=5 H=384	B=14 H=384	B=14 H=512
S4	B=2 H=768	B=3 H=768	B=3 H=1024

$\mathbb{R}^{((M^2+N) \times (M^2+N))}$  is added during attention computation:

$$Attention(Q, K, V) = \text{Softmax} \left( \frac{QK^T}{\sqrt{d}} + B \right) V. \quad (1)$$

Here,  $Q$ ,  $K$ , and  $V$  are the query, key, and value matrices of size  $\mathbb{R}^{((M^2+N) \times d)}$ , where  $M^2$  corresponds to the number of image patches and  $N$  is the count of extra tokens (e.g., class and meta tokens). The bias matrix  $\hat{B}$  is parameterized, supporting relative positions from  $-M-1$  to  $M+1$ . A shared bias is applied for non-visual tokens since their spatial position is undefined. The Relative Transformer Block comprises multi-head self-attention (MSA), layer normalization (LN), and a multi-layer perceptron (MLP), applied to the input token sequence  $z_0$ :

$$\begin{aligned} z_0 &= [x_{\text{class}}; x_{\text{meta}}^1, \dots, x_{\text{meta}}^{n-1}; x_{\text{vision}}^1, \dots, x_{\text{vision}}^m], \\ z'_i &= \text{MSA}(\text{LN}(z_{i-1})) + z_i, \\ z_i &= \text{MLP}(\text{LN}(z'_i)) + z'_i. \end{aligned} \quad (2)$$

In this formulation,  $z_i \in \mathbb{R}^{(M^2+N) \times d}$  captures the updated token sequence at each transformer layer. Stages S3 and S4 each generate a class token,  $z_{\text{class}}^1$  and  $z_{\text{class}}^2$ , which encode combined visual and meta representations. Since these tokens may differ in dimension,  $z_{\text{class}}^1$  is first projected to match the shape of  $z_{\text{class}}^2$  using an MLP. The two are then concatenated and passed through a 1D

convolution followed by normalization:

$$\begin{aligned}\hat{z}_{\text{class}}^1 &= \text{MLP}(\text{LN}(z_{\text{class}}^1)), \\ z_{\text{class}} &= \text{Conv1d}(\text{Concat}(\hat{z}_{\text{class}}^1, z_{\text{class}}^2)), \\ y &= \text{LN}(z_{\text{class}}).\end{aligned}\tag{3}$$

The final output  $y$  aggregates information across multiple scales and token types. When using external attributes as metadata, these are encoded as vectors and embedded using a fully connected non-linear function  $f : \mathbb{R}^n \rightarrow \mathbb{R}^d$ . To prevent overreliance on metadata (and potential overfitting), we apply progressive metadata masking during training, forcing the model to learn robust visual features while still leveraging auxiliary signals.

## 2.4 Experimental Settings

We compare against traditional and modern CNNs pre-trained on ImageNet [13, 14, 18–25]. All models underwent training for 100 epochs using a resolution of  $224 \times 224$  and a batch size of 32. Adam optimizer with  $lr = 10^{-3}$  was the default for baselines, AdamW with base  $lr = 10^{-4}$  for MetaFormer, and SGD with base  $lr = 10^{-2}$  for YOLO. We quantify uncertainty using 95% bootstrap confidence intervals obtained by resampling test examples with replacement (percentile method,  $B = 2000$ ). Code and the curated datasets are publicly available at <https://github.com/ammardodhi255/demographic-aware-fgvr-wrist-pathology-recognition.git>.

## 3 Results & Discussion

### 3.1 Baseline Comparison

Table 3 shows that baseline MetaFormer (vision only) outperforms widely used CNNs and more recent architectures (Swin Transformer, YOLO11s, and Conv NeXtV2-Tiny). This gives credence to the fact that transformer-based architectures with fine-grained design are better suited to capture subtle morphological cues in pediatric wrist radiographs. At the bottom, our final fusion variant yields the highest accuracy.

### 3.2 Ablation Analysis

Integrating demographic metadata improves performance across configurations (Table 4). In particular, *token fusion* consistently outperforms *vision* and *early fusion*, suggesting that injecting demographic information at the representation/token level is more effective than concatenating it at the input. Attribute-level analysis (Table 5) further indicates that both age and sex contribute independently to performance, while combining them yields the largest improvement, supporting the clinical relevance of demographic context.

Table 3: Vision-only baselines on the test set. MetaFormer fusion variant (bottom) achieve the best performance.

Model	Accuracy (%) (95% CI)
ViT	59.0 (54.0–64.1)
AlexNet	66.1 (61.3–71.2)
YOLO11s	69.5 (64.7–74.3)
VGG16	70.1 (65.5–74.9)
GoogleNet	72.9 (68.1–77.4)
ResNet50	74.0 (69.8–78.5)
DenseNet201	74.9 (70.3–79.4)
ConvNeXtV2	76.0 (71.5–80.2)
InceptionV3	77.1 (72.6–81.4)
Swin Transformer	77.4 (72.9–81.6)
EfficientNetV2	78.0 (73.7–81.9)
<b>MetaFormer (Base)</b>	<b>79.1 (74.9–83.3)</b>
<b>MetaFormer-FG-2-inat-vision (Ours)</b>	<b>79.9 (75.9–83.9)</b>
<b>MetaFormer-FG-2-inat-fusion (Ours)</b>	<b>82.2 (78.2–86.2)</b>

We selected the “FG-2” configuration and initialized it with weights pre-trained on iNaturalist [26], yielding “FG-2-inat”. This model achieves the strongest overall performance, surpassing all other configurations under both fusion strategies. Compared to ImageNet initialization, fine-grained pretraining provides a clear advantage, suggesting that supervision from fine-grained domains, where subtle inter-class differences dominate, induces representations that transfer well to pediatric wrist abnormalities.

Table 4: Joint evaluation of architecture configuration and fusion strategy reported with test accuracy (%) (95% CI).

Configuration	Vision	Early Fusion	Token Fusion (Ours)
FG-0	79.1 (74.9–83.3)	75.1 (70.6–79.7)	78.5 (74.0–82.5)
FG-1	77.4 (73.2–81.6)	<b>76.0 (71.5–80.2)</b>	79.7 (75.4–83.6)
FG-2	78.5 (74.3–82.5)	74.9 (70.3–79.4)	73.4 (68.6–78.0)
<b>FG-2-inat (Ours)</b>	<b>79.9 (75.9–83.9)</b>	75.1 (70.6–79.7)	<b>82.2 (78.2–86.2)</b>

Table 6 shows that if masking is too weak, the network can overfit to metadata-correlated shortcuts (reducing robustness when demographic priors shift). Conversely, overly strong or constant masking suppresses informative auxiliary signals and prevents the model from learning a stable joint representation. Our *progressive* masking schedule provides the best trade-off, yielding the highest test accuracy by gradually reducing metadata availability over training.

Table 5: Accuracies obtained by FG-2-inat-default configuration on metadata attributes.

Attribute	Accuracy (%) (95% CI)
Vision + Age	79.7 (75.4–83.6)
Vision + Gender	79.1 (74.9–83.3)
Vision + Age + Gender	<b>82.2 (78.2–86.2)</b>

Table 6: Effect of masking schedule and probability on test accuracy.

Mask Type	Mask Prob	Accuracy (%) (95% CI)
Constant	0.1	79.7 (75.4–83.9)
	0.2	79.1 (75.1–83.3)
	0.3	79.7 (75.1–83.6)
	0.5	79.4 (75.1–83.3)
Linear	0.1	79.7 (75.4–83.6)
	0.2	78.8 (74.6–83.1)
	0.3	78.8 (74.6–83.1)
	0.5	79.4 (75.1–83.6)
<b>Progressive (Ours)</b>	Scheduled	<b>82.2 (78.2–86.2)</b>

### 3.3 Interpretability with XAI

Grad-CAM’s output (Fig.3) show MetaFormer’s salient regions often overlap clinically relevant wrist anatomy (e.g., near suspected fractures or abnormal bone), though some maps are diffuse, suggesting imperfect localization and occasional reliance on non-pathological cues.

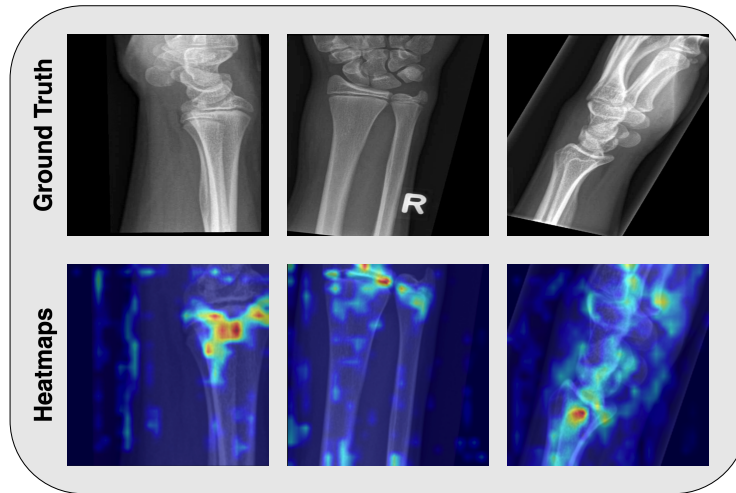


Fig. 3: Heatmaps from the final convolutional layer in stage 2 (S2) of our configuration “FG-2-inat” on a limited dataset.

Fig.4 further shows that metadata improves fracture discrimination while maintaining performance on bone anomaly and soft-tissue recognition. On the larger “Fracture vs. No Fracture” dataset (Table 7), metadata integration produced a 10% absolute gain. This gain came from being able to better distinguish “non-fracture” instances from the “fractured” ones than the baseline. These results suggest that metadata not only aids fine-grained wrist pathology recognition but also enhances scalability to larger clinical datasets.

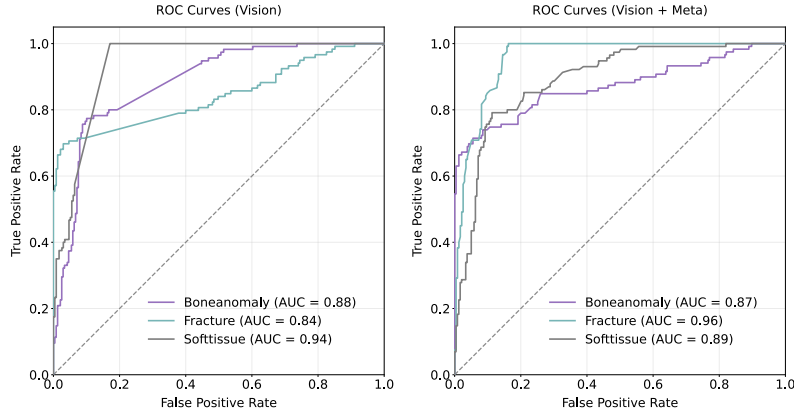


Fig. 4: ROC curves showing that metadata substantially improves fracture discrimination (AUC 0.84→0.96).

### 3.4 Failure Cases & Error Analysis

On the held-out test set ( $n = 354$ ), the most common confusions are `boneanomaly` (0)→`softtissue` (2) (25 cases) and `soft_tissue` (2)→`fracture` (1) (23 cases). Consistent with Table 8, class 0 shows high precision ( $\approx 96\%$ ) but lower sensitivity ( $\approx 62\text{--}66\%$ ), indicating conservative `boneanomaly` predictions. Class 1 attains 100% sensitivity but 75% precision, i.e., fractures are rarely missed but some non-fractures are overcalled. Accuracy decreases in older age bins ( $\approx 0.75\text{--}0.77$  for `age_norm`  $\geq 0.526$  vs.  $\approx 0.91$  for `age_norm`  $< 0.526$ ), while performance is similar across sex. Notably, some correct predictions have low confidence (median  $\approx 0.74$ ), suggesting borderline cases where clinician review may help.

Table 7: Performance evaluation on a significantly larger (fracture vs. no fracture) dataset.

FG-2-inat (Ours)	Test Accuracy (%)
Vision	50.1
Vision + Meta	<b>60.4</b>

## 4 Conclusion

Overall, our experiments demonstrate three key findings: (1) Fine-grained transformer architecture outperforms conventional and modern CNNs for pediatric wrist pathology. (2) Demographic metadata (age, sex) improves recognition across both limited and large-scale datasets. (3) Fine-grained pretraining enhances generalization compared to using ImageNet weights. These results emphasize that integrating developmental context into vision models is essential for robust pediatric musculoskeletal diagnosis.

Table 8: Evaluation of our default fusion (FG-2-inat).

Configuration	Cls	Sensitivity (%)	Specificity (%)	Precision (%)
Vision	0	62.2	98.7	96.1
	1	100.0	82.9	75.0
	2	77.4	88.3	76.1
Vision+Meta	0	66.4	98.7	96.3
	1	100.0	82.9	75.0
	2	77.4	90.4	79.5

## 5 Acknowledgement

This work was supported by the CONNECT Project NORPART-2021/10502, funded by the Norwegian Directorate for Higher Education and Skills (DIKU).

## References

1. Bryan C. MD Hoynak. Wrist Fracture Management in the ED. Practice Essentials, Pathophysiology, Prognosis, 2022.
2. Scott J Adams, Robert, Xin Yi, and Paul Babyn. Artificial intelligence solutions for analysis of x-ray images. *Canadian Association of Radiologists Journal*, 72(1):60–72, Aug 2020.
3. Dina Nur Anggraini Ningrum, Sheng-Po Yuan, Woon-Man Kung, Chieh-Chen Wu, I-Shiang Tzeng, Chu-Ya Huang, Jack Yu-Chuan Li, and Yao-Chin Wang. Deep Learning Classifier with Patient’s Metadata of Dermoscopic Images in Malignant Melanoma Detection. *Journal of Multidisciplinary Healthcare*, 14:877–885, 2021.
4. Fabrizio Nunnari, Chirag Bhuvaneshwara, Abraham Obinwanne Ezema, and Daniel Sonntag. A Study on the Fusion of Pixels and Patient Metadata in CNN-Based Classification of Skin Lesion Images. In Andreas Holzinger, Peter Kieseberg, A Min Tjoa, and Edgar Weippl, editors, *Machine Learning and Knowledge Extraction*, pages 191–208. Springer International Publishing, 2020.
5. Gan Cai, Yu Zhu, Yue Wu, Xiaoben Jiang, Jiongyao Ye, and Dawei Yang. A Multimodal Transformer to Fuse Images and Metadata for Skin Disease Classification. *The Visual Computer*, 39(7):2781–2793, 2023.
6. Spencer A. Thomas. Combining Image Features and Patient Metadata to Enhance Transfer Learning. In *2021 43rd Annual International Conference of the IEEE Engineering in Medicine and Biology Society (EMBC)*, pages 2660–2663, 2021.
7. Florian Hinterwimmer, Michael Guenther, Sarah Consalvo, Jan Neumann, Alexandra Gersing, Klaus Woertler, Rüdiger von Eisenhart-Rothe, Rainer Burgkart, and Daniel Rueckert. Impact of metadata in multimodal classification of bone tumours. *BMC Musculoskeletal Disorders*, 25(1), Oct 2024.
8. Zhen Bian, Yuan Guo, XueMin Lyu, Zheng Yang, and Jason Pui Yin Cheung. Relationship between hand and wrist bone age assessment methods. *Medicine*, 99(39):e22392, September 2020.
9. Laura S. Kox, Rik B. J. Kraan, Kees F. van Dijke, Robert Hemke, Sjoerd Jens, Milko C. de Jonge, Edwin H. G. Oei, Frank F. Smithuis, Maaïke P. Terra, and Mario Maas. Systematic assessment of the growth plates of the wrist in young gymnasts: development and validation of the amsterdam MRI assessment of the physis (AMPHYS) protocol. *BMJ Open Sport & Exercise Medicine*, 4(1):e000352, April 2018.

10. Alex F. Roche, Jean Roberts, and Peter V. V. Hamill. Skeletal maturity of children 6–11 years, united states. (140):1–62, November 1974. PMID: 4374802.
11. Bo Zhao, Jiashi Feng, Xiaogang Wu, and Shuicheng Yan. A survey on deep learning-based fine-grained object classification and semantic segmentation. *International Journal of Automation and Computing*, 14(2):119–135, 2017.
12. Ammar Ahmed, Ali Shariq Imran, Zenun Kastrati, Sher Muhammad Daudpota, Mohib Ullah, and Waheed Noor. Learning from the few: Fine-grained approach to pediatric wrist pathology recognition on a limited dataset. *Computers in Biology and Medicine*, 181:109044, 2024.
13. Sanghyun Woo, Shoubhik Debnath, Ronghang Hu, Xinlei Chen, Zhuang Liu, In So Kweon, and Saining Xie. Convnext v2: Co-designing and scaling convnets with masked autoencoders, 2023.
14. Glenn Jocher, Jing Qiu, and Ayush Chaurasia. Ultralytics YOLO, January 2023.
15. Yin Cui, Yang Song, Chen Sun, Andrew Howard, and Serge Belongie. Large scale fine-grained categorization and domain-specific transfer learning, 2018.
16. Eveline Nagy, Martin Janisch, Filip Hrzić, Guilherme Aresta, Horst Bischof, et al. A pediatric wrist trauma x-ray dataset (grazpedwri-dx) for machine learning. *Scientific Data*, 9:222, 2022.
17. Qishuai Diao, Yi Jiang, Bin Wen, Jia Sun, and Zehuan Yuan. MetaFormer: A Unified Meta Framework for Fine-Grained Recognition. *arXiv.org*, 2022.
18. Jia Deng, Wei Dong, Richard Socher, Li-Jia Li, Kai Li, and Li Fei-Fei. Imagenet: A large-scale hierarchical image database. In *Proceedings of the IEEE Conference on Computer Vision and Pattern Recognition (CVPR)*, pages 248–255. IEEE, 2009.
19. Alexey Dosovitskiy, Lucas Beyer, Alexander Kolesnikov, Dirk Weissenborn, Xi-aohua Zhai, Thomas Unterthiner, Mostafa Dehghani, Matthias Minderer, Georg Heigold, Sylvain Gelly, Jakob Uszkoreit, and Neil Houlsby. An Image is Worth 16x16 Words: Transformers for Image Recognition at Scale. 2020.
20. Mingxing Tan and Quoc V. Le. EfficientNetV2: Smaller Models and Faster Training. 2021.
21. Alex Krizhevsky, Ilya Sutskever, and Geoffrey E. Hinton. ImageNet Classification with Deep Convolutional Neural Networks. In *Advances in Neural Information Processing Systems*. 2012.
22. Gao Huang, Zhuang Liu, Laurens van der Maaten, and Kilian Q. Weinberger. Densely Connected Convolutional Networks. 2018.
23. Christian Szegedy, Wei Liu, Yangqing Jia, Pierre Sermanet, Scott Reed, Dragomir Anguelov, Dumitru Erhan, Vincent Vanhoucke, and Andrew Rabinovich. Going deeper with convolutions. In *2015 IEEE Conference on Computer Vision and Pattern Recognition (CVPR)*, pages 1–9. IEEE, 2015.
24. Kaiming He, Xiangyu Zhang, Shaoqing Ren, and Jian Sun. Deep Residual Learning for Image Recognition. 2015.
25. Ze Liu, Yutong Lin, Yue Cao, Han Hu, Yixuan Wei, Zheng Zhang, Stephen Lin, and Baining Guo. Swin Transformer: Hierarchical Vision Transformer using Shifted Windows. *arXiv preprint*, 3 2021. arXiv:2103.14030.
26. Grant Van Horn, Oisin Mac Aodha, Yang Song, Yin Cui, Chen Sun, Alex Shepard, Hartwig Adam, Pietro Perona, and Serge Belongie. The iNaturalist Species Classification and Detection Dataset. *arXiv.org*, April 2018.